

# Gravitational Lens Modeling of Doubly Imaged Quasars: A Pathway to Determining the Hubble Constant

AN UNDERGRADUATE HONORS THESIS BY

RYAN BRADY,<sup>1</sup>

PROJECT ADVISOR: PROFESSOR SIMON BIRRER

PRESENTED IN PARTIAL FULFILLMENT OF THE REQUIREMENTS  
FOR GRADUATION IN ASTRONOMY WITH HONORS FROM STONY BROOK UNIVERSITY

<sup>1</sup>*Department of Physics and Astronomy, Stony Brook University, Stony Brook, NY 11794-3800, USA*

## ABSTRACT

We present gravitational lens models for six doubly imaged quasars observed with the Hubble Space Telescope F814W and F475X bands, produced using the open source suite `Lenstronomy`, in the first phase of a hierarchical study to further constrain the Hubble constant with time-delay cosmography. Our modeling pipeline incorporates a two-stage optimization procedure using Particle Swarm Optimization, followed by iterative point spread function reconstruction and Markov Chain Monte Carlo sampling, to ensure robust fits and accurate uncertainty quantification. In the F814W band, lens galaxies are well described by Sérsic profiles with indices  $n = 1.71$  to  $n = 5.96$  and effective radii of  $0.40''$  to  $2.31''$ , consistent with early-type morphologies. Mass models yield Einstein radii between  $0.753''$  and  $1.517''$ , and little external shear ( $\gamma \sim 0.03$ – $0.20$ ). Photometric analyses show lens galaxies with expected color gradients, appearing systematically fainter in the F475X band, and quasar image flux ratios indicate possible microlensing and differential extinction effects. Three systems (J0806+2006, J1620+1203, and J2325-5229) display extended host galaxy emission, further constraining the mass models and indicating source profiles consistent with irregular morphologies. Astrometric measurements confirm well-separated image configurations with separations of  $1.49''$ – $2.82''$ , aligning with typical galaxy-scale lenses. Using the best-fit lens mass and point source models in the F814W band, the Fermat potential and time delay differences between the quasar images are calculated. Four out of five calculated time delays are within  $1\sigma$  of observationally derived values for a flat  $\Lambda$ CDM cosmology, with one system not yet having published observational data, validating the robustness of the modeling pipeline. The next phase of this work will involve combining the best-fit Fermat potential differences between quasar images with the measured time delays in a hierarchical framework to yield transparent and robust calculations of the Hubble constant.

*To my grandmother*

## 1. INTRODUCTION

Today, the  $\Lambda$  Cold Dark Matter ( $\Lambda$ CDM) cosmological model serves as the prevailing framework to describe the Universe on the largest scales. Within this paradigm, the Universe is composed predominantly of cold dark matter and dark energy, the latter manifesting as a cosmological constant ( $\Lambda$ ) responsible for its accelerated expansion (Weinberg et al. 2013). Precise measurement of the Hubble constant ( $H_0$ ) remains central to this model, as it sets the scale for cosmic distances and expansion history.

Despite the successes of  $\Lambda$ CDM in explaining a wide range of cosmological observations, a persistent and statistically significant discrepancy has appeared in recent years between measurements of  $H_0$  derived from observations of the early Universe and those from the local Universe. Measurements of the cosmic microwave background (CMB) anisotropies by the *Planck* satellite, when interpreted within the  $\Lambda$ CDM framework, yield a value of  $H_0 = 67.4 \pm 0.5 \text{ km s}^{-1} \text{ Mpc}^{-1}$  (Planck Collaboration et al. 2020). In contrast, direct distance ladder measurements, such as those conducted by the SH0ES collaboration using Cepheid-calibrated Type Ia supernovae, report a significantly higher value of  $H_0 = 73.04 \pm 1.04 \text{ km s}^{-1} \text{ Mpc}^{-1}$  (Riess et al. 2022). This discrepancy, often referred to as the “Hubble tension,” now exceeds the  $5\sigma$  threshold and suggests either unknown systematic errors in one or more of the measurement techniques or, more provocatively, the need for new physics beyond  $\Lambda$ CDM (Di Valentino et al. 2021).

Time-delay cosmography (TDC) of strongly lensed quasars has emerged as an independent and complementary method for determining  $H_0$  that circumvents many of the systematics inherent in other techniques (Birrer et al. 2024). In gravitational lensing, the lens equation assumes the thin lens approximation, where all the mass of the lens is projected onto a two-dimensional plane perpendicular to the line of sight. Under this approximation, the bending of light is considered to occur instantaneously at the lens plane. The source plane, where the true position of the background object lies, is then mapped to the image plane, where we observe the lensed images. Let  $\vec{\theta}$  represent the observed angular position of a gravitationally lensed image, and  $\vec{\beta}$  be the true (unlensed) position of the background source. The relationship between these coordinates is described as:

$$\vec{\beta} = \vec{\theta} - \vec{\alpha}(\vec{\theta}), \quad (1)$$

where  $\vec{\alpha}(\vec{\theta})$  is the deflection angle that distorts  $\vec{\beta}$ . The deflection angle is given by the gradient of the effective lensing potential  $\psi(\vec{\theta})$ :

$$\vec{\alpha}(\vec{\theta}) = \nabla \psi(\vec{\theta}), \quad (2)$$

where  $\psi(\vec{\theta})$  is related to the projected surface mass density (or convergence)  $\kappa(\vec{\theta})$  of the lens via the Poisson equation:

$$\nabla^2 \psi(\vec{\theta}) = 2\kappa(\vec{\theta}). \quad (3)$$

Lensing also alters the apparent brightness of the source via magnification. The magnification tensor is determined by the Jacobian matrix,  $\mathbf{A}$ , of the lens equation:

$$\mathbf{A} = \frac{\partial \vec{\beta}}{\partial \vec{\theta}} = \mathbb{I} - \frac{\partial \vec{\alpha}}{\partial \vec{\theta}}. \quad (4)$$

The total magnification of an image is given by the determinant of the inverse of this matrix:

$$\mu = \frac{1}{\det(\mathbf{A})} = \frac{1}{(1 - \kappa)^2 - \gamma^2}, \quad (5)$$

where  $\gamma$  is the shear, which describes the tidal gravitational field of the lens that distorts the shape of background sources. The condition  $\det(\mathbf{A}) = 0$  defines critical curves in the image plane, where magnification formally diverges. These curves map to caustics in the source plane, which delineate regions where the number of lensed images of a source changes. Sources located near or on caustics experience extreme magnification, often leading to observable phenomena such as arcs and Einstein rings.

First proposed by Refsdal (1964), TDC relies on the fact that multiple images of a background quasar, lensed by a foreground galaxy, arrive at the observer at different times due to differences in both the geometric path length and the gravitational potential traversed by the light rays. Fermat’s principle in gravitational lensing states that the light follows paths that extremize the arrival time function:

$$t(\vec{\theta}) = \frac{1 + z_l}{c} \left[ \frac{D_l D_s}{D_{ls}} \left( \frac{1}{2} (\vec{\theta} - \vec{\beta})^2 - \psi(\vec{\theta}) \right) \right], \quad (6)$$

where  $z_l$  is the redshift of the lens,  $D_l$  is the luminosity distance to the lens,  $D_s$  is the luminosity distance to the source, and  $D_{ls}$  is the luminosity distance between the lens and the source. The time delay between two images, labeled A and B, is then given by:

$$\Delta t_{AB} = \frac{D_{\Delta t}}{c} \Delta \Phi_{AB}(\zeta_{\text{lens}}), \quad (7)$$

where  $\Delta \Phi_{AB}$  is the Fermat potential difference between the images as a function of the lens mass parameters  $\zeta_{\text{lens}}$ . The time delay distance,  $D_{\Delta t}$ , is defined as:

$$D_{\Delta t} = (1 + z_l) \frac{D_l D_s}{D_{ls}}, \quad (8)$$

which scales inversely with  $H_0$ :

$$H_0 \propto \frac{1}{D_{\Delta t}} \propto \frac{c \Delta t_{AB}}{\Delta \Phi_{AB}(\zeta_{\text{lens}})}. \quad (9)$$

Therefore, measurements of time delays between quasar images and accurate Fermat potential models provide a direct way to infer  $H_0$ .

The H0LiCOW collaboration has applied this technique to a sample of six well-characterized quadruply imaged quasar systems and reported values of  $H_0$  consistent with the local distance ladder measurements, finding  $H_0 = 73.3^{+1.7}_{-1.8} \text{ km s}^{-1} \text{ Mpc}^{-1}$  (Wong et al. 2020). Similarly, Birrer et al. (2019) measure  $H_0 = 72.5^{+2.1}_{-2.3} \text{ km s}^{-1} \text{ Mpc}^{-1}$  via an analysis of the doubly imaged quasar SDSS 1206+4332. These results reinforce the observed tension and emphasize the potential for time-delay cosmography to arbitrate between the competing measurements of  $H_0$  and to probe possible extensions to the standard cosmological model.

While the ultimate goal of time-delay cosmography is a precise and accurate determination of  $H_0$ , the cornerstone of this technique lies in the construction of reliable gravitational lens models. In this work, we concentrate on detailed modeling of the mass and light distributions for a sample of six doubly imaged quasar systems observed with the *Hubble Space Telescope* (HST). By developing a uniform modeling pipeline, we extract the key lensing parameters, such as the Einstein radius and external shear, that will ultimately be used in conjunction with measured time delays to infer  $H_0$ . This paper represents the first stage of a hierarchical approach: we isolate the lens modeling to ensure the accuracy and internal consistency of  $\zeta_{\text{lens}}$  before incorporating the time-delay measurements and propagating uncertainties into cosmographic inference. This strategy mirrors the approach of recent modeling efforts such as STRIDES (Schmidt et al. 2023), which emphasized automation and uniformity to handle large lens samples efficiently.

Our focus on doubles complements these efforts and highlights a scalable path forward for time-delay cosmography using the most prevalent lensing configurations. While quadruply imaged quasars provide more constraints per system—from multiple image positions and flux ratios—they are relatively rare and often involve complex environments with group or cluster-scale lensing potentials, blending of multiple lens galaxies, or perturbers along the line of sight (Liao et al. 2015; Suyu et al. 2017). Doubly imaged systems, by contrast, are more abundant and typically involve simpler lens configurations with fewer deflectors and lower environmental shear (Oguri & Marshall 2010; More et al. 2012). Despite having fewer observational constraints, the modeling of doubles offers several advantages: it reduces the number of degrees of freedom, simplifies the interpretation of degeneracies (e.g., mass-sheet and source-

position transformations), and can achieve high modeling precision when host galaxy light or external data are available. With the advent of large-scale surveys yielding thousands of lens candidates, a robust modeling framework for doubles is critical to maximizing their full cosmographic potential.

In Section 2, we present the discoveries and relevant cosmological information for the six doubly imaged systems in the study. Section 3 details the Lenstronomy modeling pipeline and system modeling choices. The reconstructions of all six systems in the F814W band and for four systems in the F475X band are presented in Section 4, alongside derived astrometry and photometry. We discuss some systematic uncertainties in Section 5, and conclude the study in Section 6.

## 2. HST SAMPLES

Each lens was observed in three HST filters with the Wide Field Camera 3 (WFC3): F160W for infrared (IR) data, and F475X and F814W for ultraviolet-visual (UVIS) data. To enhance data sampling, a 4-point dither pattern was used for IR observations, while a 2-point dither pattern was applied for UVIS exposures, with both long and short exposures taken at each dither position. For data reduction, alignment, and combination of exposures in each filter, we utilized the Python package `AstroDrizzle` (Avila et al. 2015). The final reduced images have a pixel scale of  $0.08''/\text{pixel}$  for IR exposures and  $0.04''/\text{pixel}$  for UVIS exposures. RGB composites of the six systems of study are shown in Figure 1.

### 2.1. Notes on Individual Doubles

This section provides a brief description of the six doubly lensed systems studied in this analysis.

#### 2.1.1. J0407-5006

This lens was identified as part of the STRIDES 2016 follow-up campaign by Treu et al. (2018) and Anguita et al. (2018). Spectroscopic observations were obtained using the New Technology Telescope (NTT) equipped with EFOSC2, confirming the lensing nature of the system. The spectra of both image components establish a source redshift of  $z_s = 1.515$ . The lens galaxy redshift has not yet been spectroscopically confirmed but is estimated photometrically to be  $z_l \sim 0.55$ .

#### 2.1.2. J0806+2006

This system was identified from the Sloan Digital Sky Survey (SDSS) spectroscopic quasar sample. Follow-up imaging was conducted by Inada et al. (2006) in optical and near-infrared bands using the University of Hawaii

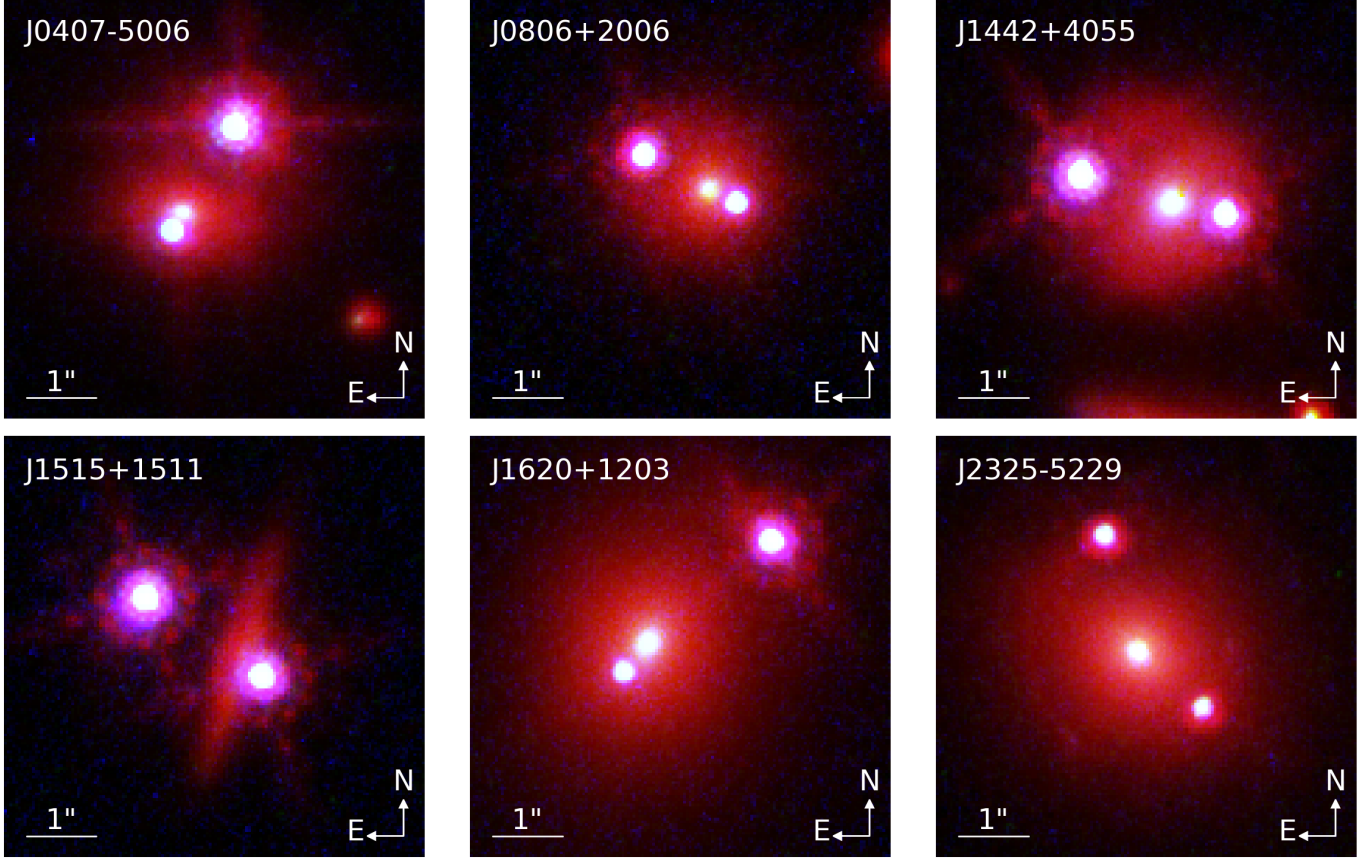


**Figure 1.** Composite red-green-blue (RGB) images of the six doubly imaged quasar systems used in our analysis. Each figure presents an image constructed from the HST observations, with F160W data mapped to the red channel, F814W data to the green channel, and F475X data to the blue channel. To enhance visualization, the intensity scaling of each band is adjusted individually.

88-inch (UH88) telescope and the Keck I telescope, confirming the presence of a lensing galaxy. Spectroscopic observations with Keck II further verified the lensing hypothesis, revealing two quasar components with identical redshifts of  $z_s = 1.540$ . The lens galaxy has an estimated redshift of  $z_l \sim 0.573$  based on a detected Mg II absorption system and photometric properties.

### 2.1.3. *J1442+4055*

*J1442+4055* was identified as a potential gravitationally lensed quasar from SDSS spectroscopic data and was confirmed through follow-up observations by Shalyapin & Goicoechea (2019). Spectroscopic analysis of the lensing galaxy using the Gran Telescopio Canarias (GTC) determined a lens redshift of  $z_l = 0.284$ , while the quasar source redshift was measured as  $z_s = 2.593$ . The system also contains a secondary intervening galaxy and an absorber at  $z \sim 1.946$ , which exhibits a strong 2175Å extinction feature, indicating the presence of dust. Mass modeling suggests external shear influences from the neighboring structures.

### 2.1.4. *J1515+1511*

This lens was identified as a doubly imaged quasar in the SDSS and confirmed through follow-up observations by Shalyapin & Goicoechea (2017). Spectroscopic observations using the GTC determined a source redshift of  $z_s = 2.049$ . While the lens galaxy redshift was initially uncertain, absorption features in the spectrum of image B suggest  $z_l = 0.742$ .

### 2.1.5. *J1620+1203*

*J1620+1203* was identified as a lensed quasar as part of the Sloan Digital Sky Survey Quasar Lens Search (SQLS) (Kayo et al. 2010). Follow-up imaging using the Faint Object Camera and Spectrograph (FOCAS) on the Subaru Telescope determined that the source quasar has a redshift of  $z_s = 1.158$ , while the lensing galaxy redshift was determined as  $z_l = 0.398$  based on detected absorption features.

### 2.1.6. *J2325-5229*

*J2325-5229* was discovered as a gravitationally lensed quasar in the VISTA Hemisphere Survey (VHS) and

DES using a morphology-independent machine learning technique (Ostrovski et al. 2017). The foreground elliptical galaxy redshift was determined to be  $z_l = 0.400$ . Spectroscopic follow-up observations were conducted using NTT with EFOSC2, as well as archival data from the Anglo-Australian Telescope (AAT). These observations confirmed the quasar source redshift as  $z_s = 2.739$ .

### 3. LENS MODELING PROCEDURE

All lens models and fittings were developed using the publicly available Python-based and open source gravitational lens modeling suite **Lenstronomy** (Birrer & Amara 2018). Each model was constructed using 20 cores of an Intel Xeon E5-2683v3 CPU on the Stony Brook University Seawulf supercomputing cluster.

#### 3.1. Model Choices

The mass distribution of the lensing galaxy is modeled as a Singular Isothermal Ellipsoid (SIE), where the convergence at position  $\theta$  is given by:

$$\kappa(\theta_1, \theta_2) = \frac{\theta_E}{2} \frac{1}{\sqrt{q\theta_1^2 + \theta_2^2/q}}. \quad (10)$$

Here,  $\theta_E$  is the Einstein radius and  $q$  is the minor/major axis ratio. The SIE provides a flexible representation of the lensing mass distribution. Any additional linear distortions to the lensed structure caused by line-of-sight perturbers are modeled using an external shear component, characterized by a strength parameter:

$$\gamma_{\text{ext}} = \sqrt{\gamma_{\text{ext},1}^2 + \gamma_{\text{ext},2}^2}, \quad (11)$$

with position angle

$$\phi_{\text{ext}} = \frac{1}{2} \arctan(\gamma_{\text{ext},2}, \gamma_{\text{ext},1}) \quad (12)$$

The source and lens light profiles are parameterized using an elliptical Sérsic function:

$$I(R) = I_e \exp\left(-b_n\left[\left(\frac{R}{R_S}\right)^{\frac{1}{n}} - 1\right]\right), \quad (13)$$

where  $R = \sqrt{q\theta_1^2 + \theta_2^2/q}$ ,  $I_e$  the intensity at the effective radius  $R_S$ , and  $b_n$  a constant dependent on the Sérsic index  $n$ , ensuring that  $R_S$  encloses half of the total light.

Lastly, the quasar images are modeled as point sources using a point spread function (PSF) reconstructed with STARRED (Millon et al. 2024). STARRED reconstructs the PSF by jointly modeling multiple stars in the field, separating the scene into point-source and extended components. It performs a sparsity-regularized deconvolution, exploiting subpixel dithering across exposures and applying a wavelet-based prior to iteratively refine the PSF.

#### 3.2. Modeling Routine

The modeling procedure follows a systematic approach to ensure a robust and accurate reconstruction of the lens system. This routine consists of several key stages, each designed to progressively refine the model parameters and optimize the fit to the observed data.

**Data Preparation and PSF Initialization**—The analysis begins with the preparation of the observational data. The science image is loaded from a FITS file, and the pixel grid is defined with a pixel scale of  $0.04''/\text{pixel}$ . The astrometric transformation matrix is computed from the FITS header to map between pixel coordinates and celestial coordinates. The PSF is then initialized using a pixel-based representation, extracted from the empirical PSF model. To enhance accuracy, the PSF is supersampled by a factor of three to better capture the small-scale structure of the point sources.

**Initial Parameter Estimations & Constraints**—To provide a reasonable starting point for the model fitting, initial estimates of key parameters are obtained. The Einstein radius is approximated as half the observed separation between the quasar images. The lens mass profile, Sérsic indices, and ellipticities are assigned plausible values based on prior astrophysical knowledge, while initial guesses for the quasar image positions are obtained based on their coordinates in the pixel grid. Uncertainties in these parameters are accounted for by defining prior probability distributions that guide the fitting process. Furthermore, the position parameters of the lens mass and light profiles are joined, as well as the position parameters of the source light and quasar image point sources.

**Initial PSO and PSF Reconstruction**—The fitting procedure is executed in multiple stages to ensure convergence to an optimal solution. First, a Particle Swarm Optimization (PSO) algorithm is employed with 100 particles for 100 iterations to explore the parameter space and identify a set of candidate solutions. The PSO efficiently navigates complex, high-dimensional parameter landscapes by iteratively adjusting particle positions based on their fitness relative to the data. Following this global search, an iterative PSF reconstruction step is performed to refine the quasar image residuals. The best-fit model from the PSO is used here to subtract extended components such as the lens and host galaxy light, isolating the quasar residuals. These residuals are then extracted and combined to update the PSF estimate, refining the empirical representation. To ensure robustness against outliers, the “median” stacking method is applied, preventing contamination from poor

subtractions or asymmetric structures. The updated PSF is re-applied to the model, and the process continues for 500 iterations until the residuals stabilize, improving the accuracy of the quasar flux and position estimates. This self-consistent approach accounts for PSF variations not captured in the initial model, ultimately enhancing the precision of each system's reconstruction.

**Final PSO and MCMC Sampling**—After the initial PSO and PSF reconstruction, a second round of optimization is performed. The PSO is now run for up to 500 iterations to ensure a thorough exploration of the parameter space. A subsequent PSF reconstruction is carried out to minimize systematic errors and ensure that PSF misestimation does not bias the inferred lens and source properties. This PSO-PSF alternation at 500 iterations each is executed a total of four times, with the ladder two utilizing 200 particles. Following this, a final PSO is performed with 200 particles for 1000 iterations to ensure convergence, with a final PSF reconstruction ascertained to resolve any further PSF misestimations. The best-fit model from this final PSO stage is then used as the starting point for Markov Chain Monte Carlo (MCMC) sampling using the `emcee` library (Foreman-Mackey et al. 2013). The MCMC process refines the parameter estimates by generating posterior distributions, providing statistical constraints on the non-linear free model components. The MCMC is performed for 500 burn-in and 1000 run iterations, with a walker ratio of 10 for a total of 190 walkers.

**Final Model Evaluation and Residual Analysis**—Once the MCMC sampling has converged, the final best-fit parameters are used to generate a reconstructed model of the system. This model is subtracted from the observed image to produce a residual map, which is inspected for any systematic deviations or significant residual structures. The reduced chi-squared ( $\chi^2$ ) statistic is computed to assess the overall goodness-of-fit. The model is considered successful if the residuals are minimized with a reduced  $\chi^2 < 1.5$ , indicating a statistically consistent fit to the data. This multi-phase approach ensures a robust and reproducible analysis of the lens systems.

#### 4. RESULTS

For this work, we focused on independently modeling the datasets obtained using the F814W and F475X bands. The lens modeling procedure described in Section 3.2 yielded robust reconstructions of the systems with high-fidelity fits to the observational data. The reconstructed images, residuals, and magnification maps for all six systems in the F814W band and for four systems in the F475X band are shown in Figure 2 and Figure

3, respectively. Lastly, Figure 4 displays the source light profiles of the three lensing systems with extended structure.

##### 4.1. Lens Light and Mass Profiles

A summary of lens light and mass best-fit parameters are presented in Table 1 and Table 2, respectively. The lens galaxies exhibit Sérsic indices ranging from  $n = 1.71$  to  $n = 5.97$ , with most lenses favoring values close to  $n = 4$ , consistent with elliptical galaxy morphologies. The effective radii of the lenses vary from  $R_{\text{Sérsic}} = 0.40''$  to  $R_{\text{Sérsic}} = 2.31''$ , with ellipticities between  $q = 0.226$  and  $q = 0.937$ .

Lens light models were also fitted in the F475X band for systems where high-quality data were available. The F475X results generally show slightly smaller effective radii and lower Sérsic indices compared to F814W, although the overall structural parameters remain broadly consistent between the two bands. This trend is expected, as the F475X filter probes bluer wavelengths that are more sensitive to younger stellar populations or subtle morphological features not as prominent in redder bands. For instance, J0806+2006 shows a decrease in Sérsic index from  $n = 3.87$  in F814W to  $n = 1.45$  in F475X, suggesting a more pronounced disk-like component at shorter wavelengths. Similarly, J1620+1203 exhibits a reduction in  $R_{\text{Sérsic}}$  from  $2.31''$  in F814W to  $1.88''$  in F475X, while maintaining a high Sérsic index indicative of a dominant spheroidal structure. Interestingly, for J1442+4055, the half-light radius increases from  $0.94''$  in the F814W model to  $1.28''$  in the F475X while maintaining the same Sérsic index within uncertainty.

The mass models for the lens galaxies, displayed in Table 2, are characterized primarily by their Einstein radii, axis ratios ( $q_{\text{mass}}$ ), and external shear strengths ( $\gamma$ ). Einstein radii range from  $\theta_E = 0.753''$  to  $\theta_E = 1.517''$  in F814W, broadly reflecting the relatively massive nature of the lensing galaxies required to produce strong lensing configurations. The axis ratios span a wide range from  $q_{\text{mass}} = 0.410$  to  $0.905$ , suggesting a diversity in the intrinsic shapes of the lens mass distributions. External shear values are generally modest ( $\gamma \sim 0.03\text{--}0.20$ ), indicating that while environmental effects and nearby perturbers are present, the primary lensing potential is dominated by the main galaxy in most cases.

Comparing the mass parameters between F814W and F475X, some systems with dual-band models exhibit modest shifts in parameters. For example, J1620+1203 shows a decrease in Einstein radius from  $1.517''$  to  $1.430''$  between F814W and F475X, while J2325-5229 shows an increase from  $1.375''$  to  $1.480''$ . Both differ-

**Table 1.** Median lens light parameters computed from the best-fit model, with the reduced  $\chi^2$  of each fit. The associated uncertainties are statistical and were calculated using the 84th and 16th percentiles.

F814W					F475X			
Lens System	$R_{\text{Sérsic}}$ [arcsec]	$n_{\text{Sérsic}}$	$q$	$\chi^2$	$R_{\text{Sérsic}}$ [arcsec]	$n_{\text{Sérsic}}$	$q$	$\chi^2$
J0407-5006	$0.40^{+0.01}_{-0.01}$	$4.85^{+0.15}_{-0.13}$	$0.664^{+0.009}_{-0.009}$	1.23	—	—	—	—
J0806+2006	$0.52^{+0.01}_{-0.01}$	$3.87^{+0.10}_{-0.09}$	$0.937^{+0.010}_{-0.010}$	1.06	$0.24^{+0.03}_{-0.06}$	$1.45^{+0.32}_{-0.38}$	$0.695^{+0.051}_{-0.046}$	1.31
J1442+4055	$0.94^{+0.01}_{-0.01}$	$5.97^{+0.02}_{-0.04}$	$0.821^{+0.005}_{-0.005}$	1.26	$1.28^{+0.04}_{-0.04}$	$5.98^{+0.02}_{-0.03}$	$0.901^{+0.017}_{-0.015}$	1.11
J1515+1511	$0.56^{+0.03}_{-0.02}$	$1.71^{+0.09}_{-0.08}$	$0.226^{+0.004}_{-0.004}$	1.45	—	—	—	—
J1620+1203	$2.31^{+0.12}_{-0.10}$	$5.60^{+0.12}_{-0.10}$	$0.775^{+0.004}_{-0.004}$	1.08	$1.88^{+0.13}_{-0.13}$	$5.96^{+0.03}_{-0.06}$	$0.673^{+0.015}_{-0.017}$	1.16
J2325-5229	$1.11^{+0.03}_{-0.03}$	$4.37^{+0.08}_{-0.08}$	$0.835^{+0.005}_{-0.005}$	1.01	$0.79^{+0.05}_{-0.05}$	$3.74^{+0.20}_{-0.21}$	$0.871^{+0.017}_{-0.017}$	1.05

**Table 2.** Median lens mass parameters computed from the best-fit model. The associated uncertainties are statistical and were calculated using the 84th and 16th percentiles.

F814W				F475X		
Lens System	$\theta_E$ [arcsec]	$q_{\text{mass}}$	$\gamma_{\text{ext}}$	$\theta_E$	$q_{\text{mass}}$	$\gamma_{\text{ext}}$
J0407-5006	$0.82^{+0.01}_{-0.01}$	$0.80^{+0.07}_{-0.06}$	$0.08^{+0.02}_{-0.03}$	—	—	—
J0806+2006	$0.75^{+0.01}_{-0.02}$	$0.90^{+0.05}_{-0.08}$	$0.03^{+0.03}_{-0.02}$	$0.74^{+0.16}_{-0.04}$	$0.66^{+0.14}_{-0.11}$	$0.08^{+0.22}_{-0.04}$
J1442+4055	$1.17^{+0.01}_{-0.01}$	$0.80^{+0.04}_{-0.03}$	$0.08^{+0.02}_{-0.01}$	$1.08^{+0.01}_{-0.01}$	$0.51^{+0.02}_{-0.02}$	$0.21^{+0.01}_{-0.01}$
J1515+1511	$0.92^{+0.01}_{-0.01}$	$0.41^{+0.02}_{-0.02}$	$0.20^{+0.02}_{-0.02}$	—	—	—
J1620+1203	$1.52^{+0.03}_{-0.04}$	$0.67^{+0.06}_{-0.05}$	$0.08^{+0.02}_{-0.02}$	$1.43^{+0.02}_{-0.03}$	$0.66^{+0.05}_{-0.04}$	$0.14^{+0.02}_{-0.02}$
J2325-5229	$1.38^{+0.01}_{-0.01}$	$0.62^{+0.03}_{-0.02}$	$0.15^{+0.02}_{-0.02}$	$1.48^{+0.04}_{-0.08}$	$0.65^{+0.03}_{-0.03}$	$0.08^{+0.02}_{-0.01}$

ences exceed the quoted uncertainties, potentially reflecting subtle changes in the mass modeling driven by differences in image quality, the bluer band’s sensitivity to small-scale structure, or degeneracies in the fitting process. In contrast, J1442+4055 displays a more pronounced change in ellipticity and external shear, suggesting a stronger wavelength-dependent effect. While the true mass distribution of the lens galaxies should, in principle, be independent of observing band, practical factors—such as band-dependent lens light profiles or inconsistent PSF accuracy—can introduce variations. Overall, the reasonable consistency of parameters across bands supports the robustness of the modeling framework.

#### 4.2. Astrometry and Quasar Image Configuration

The relative astrometric positions of the lensing galaxies and quasar images are presented in Table 3 based upon fits of the F814W data. All systems exhibit well-separated image pairs with angular separations ranging from  $1.49''$  (J0806+2006) to  $2.82''$  (J2325-5229). These separations are broadly consistent with expectations for galaxy-scale strong lensing events. The image positions also show noticeable asymmetries relative to the deflector centers, highlighting the non-collinear and often skewed geometry of lensing configurations. These asymmetries arise from a combination of lens ellipticity, external shear, and position of the source quasar behind the deflecting galaxy. Systematic uncertainty in astrom-

etry due to sub-pixel errors in the PSF are discussed in Section 5.1.

#### 4.3. Photometry and Flux Ratios

The calculated AB magnitudes for both the lens galaxies and quasar images are presented in Table 4. Associated uncertainties for these measurements come from two quantities: statistical uncertainty from the MCMC chain and an additional zero point photometric uncertainty of WFC3 that is of value  $\pm 0.02$  mag (Bajaj et al. 2020). As can be seen, this zero point uncertainty is the dominant aspect of the total uncertainty. In the F814W band, which traces older stellar populations, the lens galaxies exhibit a broad range of magnitudes, spanning from  $m_{\text{lens}} = 18.94$  (J1620+1203) to  $m_{\text{lens}} = 21.44$  (J1515+1511). As expected, the brighter lenses generally correspond to more massive systems when analyzed with their best-fit effective radii and Einstein radii parameters, consistent with the established luminosity-mass relation observed in early-type galaxies (Faber & Jackson 1976).

The inclusion of F475X observations further refines this picture. In this bluer filter, lens galaxy magnitudes are systematically fainter, as anticipated due to the older stellar populations dominating these early-type galaxies, which emit less strongly at shorter wavelengths. For example, J1620+1203 shifts from  $m_{\text{lens}} = 18.93$  (F814W) to  $m_{\text{lens}} = 21.36$  (F475X), a difference of over two magnitudes. This steep drop in brightness is indicative of a

**Table 3.** Astrometric position of the deflector lens and relative positions of the quasar images, along with their projected image separation. The total uncertainty in relative astrometry is primarily driven by systematic errors arising from the sub-pixel reconstruction of the PSF and therefore is not stated.

Lens System Name	Deflector [arcsec]		Quasar Image A [arcsec]		Quasar Image B [arcsec]		Separation [arcsec]
	RA	Dec	$\Delta$ RA	$\Delta$ Dec	$\Delta$ RA	$\Delta$ Dec	
J0407-5006	3.455	-0.678	-0.157	-0.257	0.734	1.214	1.721
J0806+2006	4.191	-0.157	-0.929	0.501	0.390	-0.185	1.486
J1442+4055	4.234	-0.265	-1.300	0.394	0.757	-0.162	2.132
J1515+1511	4.556	-0.214	-1.403	0.851	0.265	-0.266	2.008
J1620+1203	3.274	-0.254	1.768	1.462	-0.339	-0.398	2.810
J2325-5229	3.795	-0.364	-0.488	1.657	0.911	-0.792	2.821

**Table 4.** Median AB magnitudes of the lens and images. Uncertainties reflect both statistical errors from the flux models (derived from the 84th and 16th percentiles) and an added zeropoint calibration uncertainty of  $\pm 0.02$  mag from HST. The total magnitude uncertainties are dominated by the zeropoint error.

F814W				F475X			
Lens System	Deflector	Image A	Image B	Deflector	Image A	Image B	
J0407-5006	$20.35^{+0.02}_{-0.02}$	$19.39^{+0.02}_{-0.02}$	$18.01^{+0.02}_{-0.02}$	--	--	--	
J0806+2006	$19.88^{+0.02}_{-0.02}$	$19.25^{+0.02}_{-0.02}$	$20.07^{+0.02}_{-0.02}$	$23.02^{+0.13}_{-0.25}$	$20.02^{+0.02}_{-0.02}$	$20.73^{+0.02}_{-0.02}$	
J1442+4055	$19.02^{+0.02}_{-0.02}$	$18.16^{+0.02}_{-0.02}$	$18.99^{+0.02}_{-0.02}$	$20.80^{+0.02}_{-0.02}$	$18.88^{+0.02}_{-0.02}$	$19.82^{+0.02}_{-0.02}$	
J1515+1511	$21.36^{+0.02}_{-0.02}$	$18.17^{+0.02}_{-0.02}$	$18.58^{+0.02}_{-0.02}$	--	--	--	
J1620+1203	$18.93^{+0.02}_{-0.02}$	$20.54^{+0.02}_{-0.02}$	$19.04^{+0.02}_{-0.02}$	$21.16^{+0.02}_{-0.02}$	$20.89^{+0.02}_{-0.02}$	$19.43^{+0.02}_{-0.02}$	
J2325-5229	$19.09^{+0.02}_{-0.02}$	$20.68^{+0.02}_{-0.02}$	$21.09^{+0.02}_{-0.02}$	$21.32^{+0.02}_{-0.02}$	$21.41^{+0.02}_{-0.02}$	$22.03^{+0.02}_{-0.02}$	

stellar population deficient in young, blue stars, supporting the early-type classification. Similarly, J1442+4055 exhibits a comparable trend, bright at  $m_{\text{lens}} = 19.02$  (F814W) but fading to  $m_{\text{lens}} = 20.81$  in F475X, consistent with passively evolving stellar populations (Sonnenfeld et al. 2013).

The quasar images themselves show significant flux variation between their respective components A and B, in both filters. In F814W, flux ratios  $f_B/f_A$  span from approximately 0.47 (J1442+4055) to 3.98 (J1620+1203), highlighting the diverse range of lensing configurations, magnifications, and potential environmental effects. For instance, J0407-5006 features a highly asymmetric flux ratio  $f_B/f_A \sim 3.57$  in the F814W, suggesting strong differential magnification, possibly combined with microlensing effects that preferentially magnify one image over the other.

When examining the F475X measurements, an even more nuanced view emerges. In general, flux ratios are broadly consistent between F814W and F475X, but with some notable differences hinting at wavelength-dependent effects. For example, in J2325-5229, the F814W flux ratio is about 0.689, while in F475X it drops slightly to  $\sim 0.560$ , suggesting that differential extinction (more severe in the blue) could be playing a minor role. Likewise, in J1620+1203, the flux ratio in F475X ( $f_B/f_A \sim 3.86$ ) appears to move slightly closer to unity

compared to F814W ( $f_B/f_A \sim 3.98$ ), which could indicate either differential extinction preferentially suppressing one image at longer wavelengths or a change in the microlensing amplification factor with wavelength.

The AB magnitudes of the quasar images themselves, independently of the ratios, offer further insights. Systems with notably bright A images—such as J1515+1511 and J1442+4055, both featuring  $m_A \sim 18.17$  and  $m_A \sim 18.16$  in F814W, respectively—suggest configurations where the A images lie close to the lens critical curve, experiencing substantial magnification. Conversely, systems such as J2325-5229 show relatively faint quasar images ( $m_A \sim 20.68$ ,  $m_B \sim 21.09$  in F814W, and even fainter in F475X), suggesting either lower intrinsic magnification, a lensing configuration farther from the critical curve, or additional attenuation from intervening dust or microlensing demagnification.

The F475X magnitudes, being consistently fainter across the sample for the quasar images, are expected given the quasars' typical spectral energy distributions, which peak in the ultraviolet but can be significantly reddened either intrinsically or through intervening material (Richards et al. 2006). Moreover, the lens galaxies themselves appear systematically fainter in F475X, with magnitudes typically two to three magnitudes fainter than in F814W. This trend is consistent with expectations for early-type lensing galaxies, which possess older

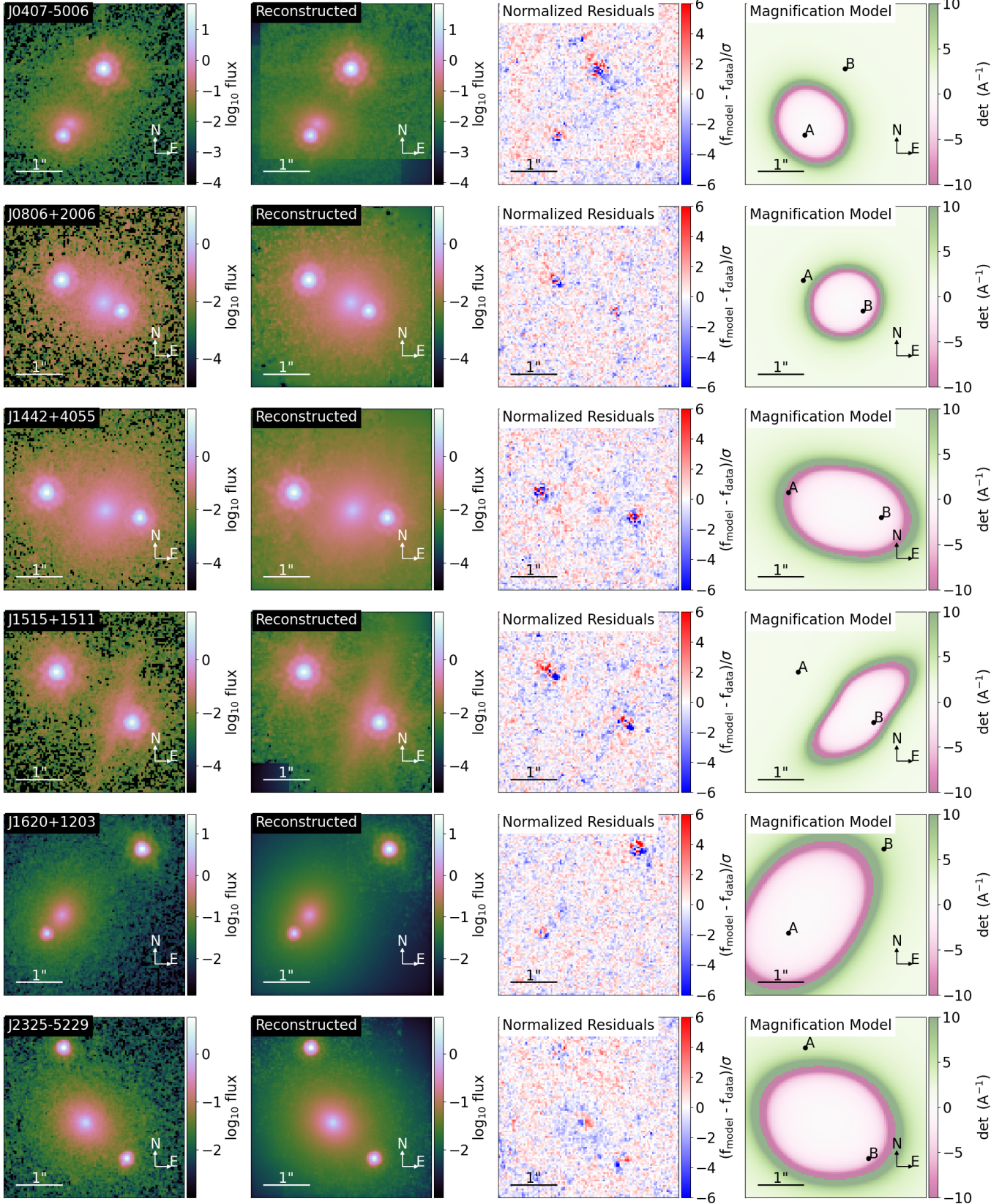


**Figure 2.** Lens Model results for all six systems in the F814W HST band. **First column:** Image cutouts of the observed lensing systems. **Second column:** Reconstructed images generated from the optimized lens model. **Third column:** Residual maps, normalized by pixel noise levels. **Fourth column:** Magnification models illustrating spatial variations in magnification.

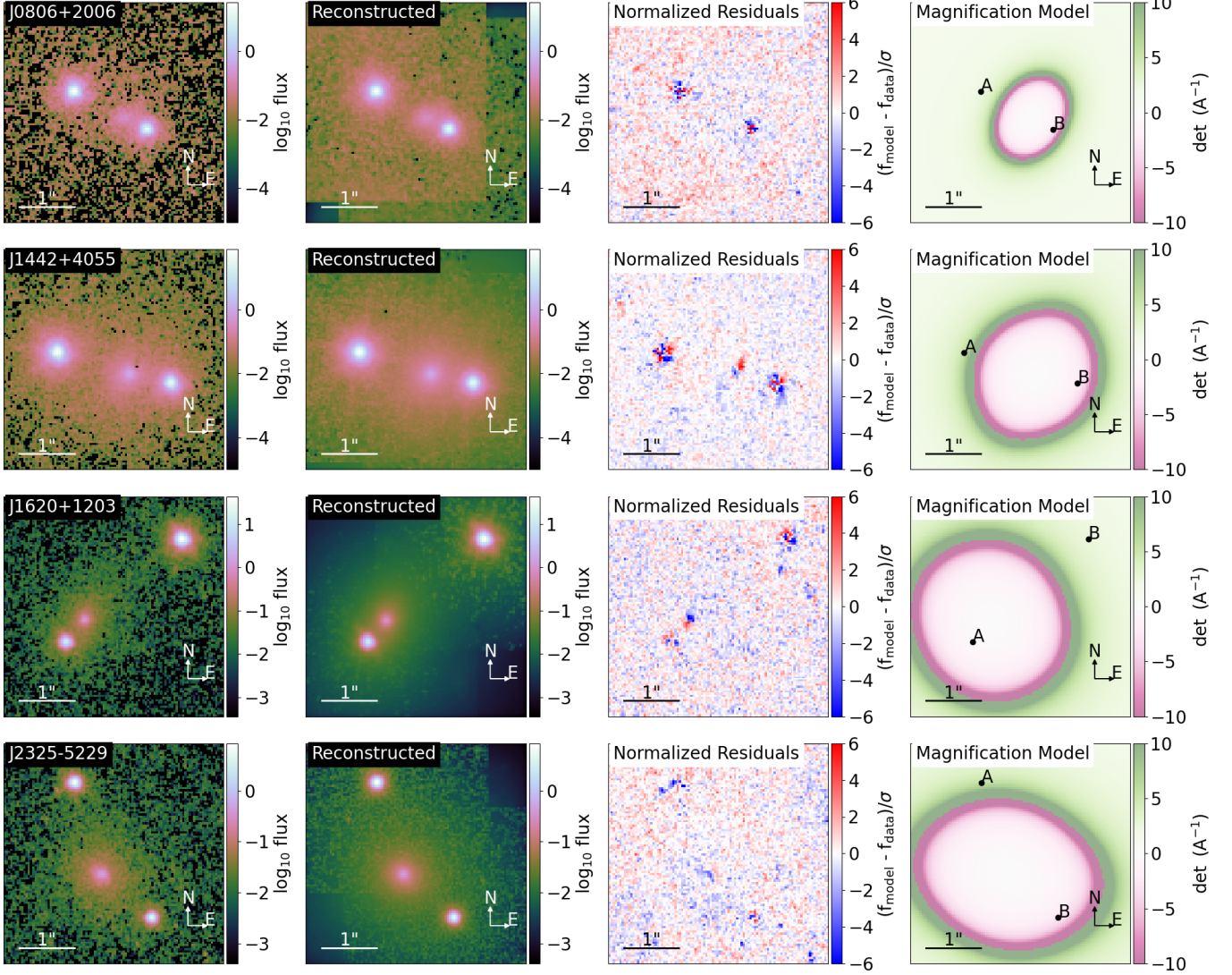


**Figure 3.** Illustration of the same components as Figure 2, but for F475X data.

stellar populations dominated by redder stars that emit less light at shorter wavelengths.

#### 4.4. Extended Source Light Profiles

Three of the six systems in our sample—J1442+4055, J1620+1203, and J2325-5229—exhibit detectable extended source emission in the F814W band, allowing us to reconstruct the host galaxy light profiles of the lensed quasars. These extended features were modeled using a Sérsic profile and jointly optimized alongside the quasar point sources and lens profiles. The reconstructed source light profiles in the image plane are shown in Figure 4.

The extended emission provides additional constraints on the source morphology and orientation, and significantly enhances the robustness of the lens model by anchoring the source position and structure beyond the quasar point sources alone. As shown in Table 5, the re-

**Table 5.** Median source light model parameters in the F814W band. The associated uncertainties are statistical and were calculated using the 84th and 16th percentiles.

Lens System	$R_{\text{Sérsic}}$ [arcsec]	$n_{\text{Sérsic}}$	$q_{\text{source}}$
J0806+2006	$0.058^{+0.005}_{-0.004}$	$0.58^{+0.11}_{-0.05}$	$0.60^{+0.08}_{-0.06}$
J1620+1203	$0.261^{+0.045}_{-0.036}$	$1.93^{+0.06}_{-0.11}$	$0.78^{+0.10}_{-0.11}$
J2325-5229	$0.050^{+0.001}_{-0.000}$	$0.52^{+0.04}_{-0.01}$	$0.81^{+0.09}_{-0.10}$

constructed source galaxies exhibit Sérsic indices ranging from  $n_{\text{Sérsic}} \sim 0.5$  to 1.9, consistent with disk-like or irregular light profiles rather than those of classical ellipticals. J0806+2006 and J2325-5229 show particularly low indices ( $n \sim 0.5$ –0.6), typical of exponential disk galaxies, while J1620+1203, with  $n \sim 1.9$ , may exhibit a more centrally concentrated, bulge-dominated

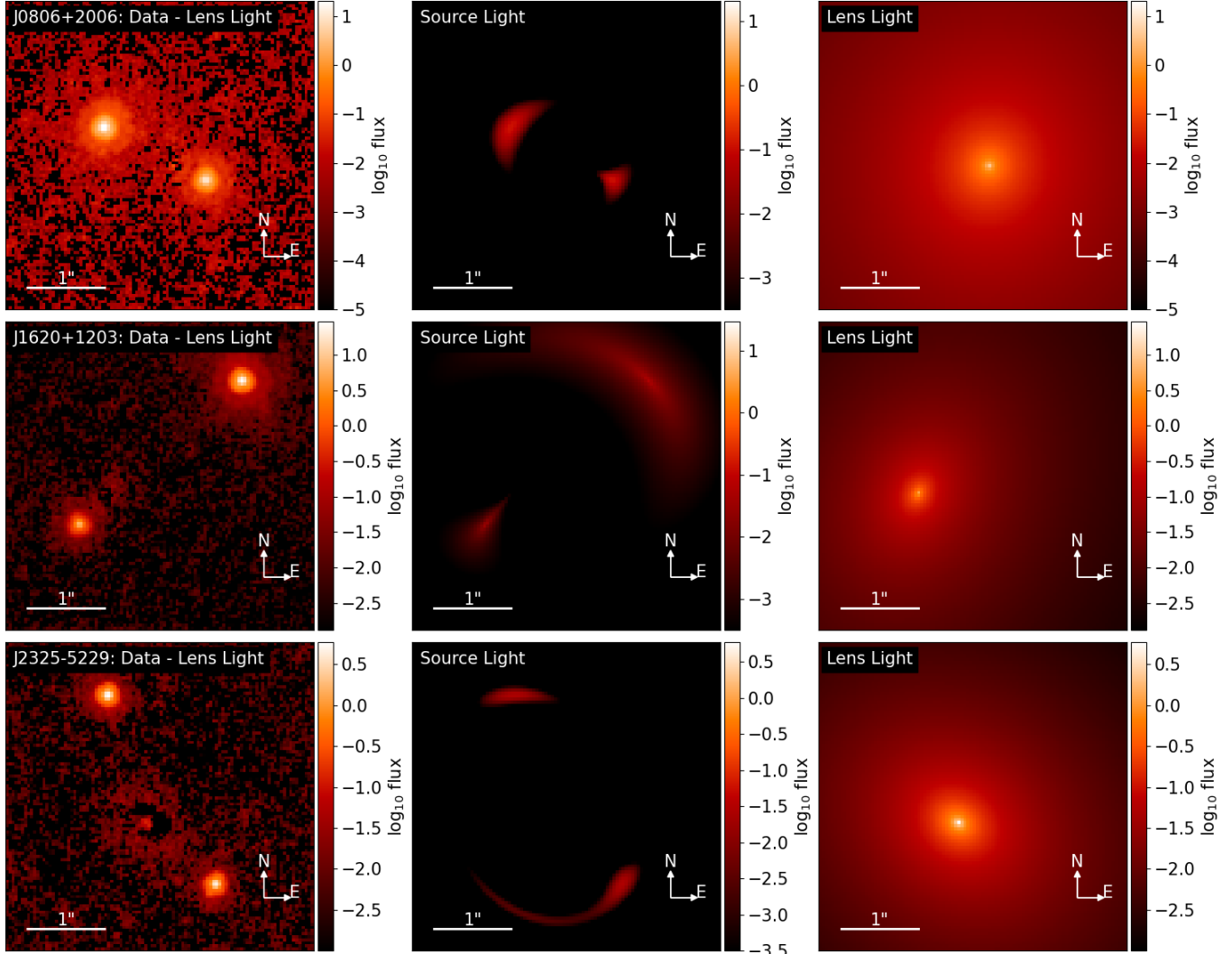


**Figure 4.** Reconstructed source and lens light models for the three lens systems which display extended source components in the F814W band. **First column:** Observed images after subtracting the best-fit lens light model. **Second column:** Best-fit source quasar light models (note: the intensity scaling is different in order to highlight the extended nature of the source components). **Third column:** Best-fit lens galaxy light models.

structure. The axis ratios, ranging from  $q_{\text{source}} = 0.60$  to  $0.81$ , suggest moderately elongated morphologies, implying the sources are not highly inclined disks or perfectly round spheroids. The half-light radii span  $0.05$  to  $0.26$  arcseconds, indicating compact but well-resolved sources. Together, these parameters suggest a diversity of intrinsic structures among the source galaxies, spanning from irregular or disk-like to more centrally concentrated systems.

These findings stand in contrast to the lens galaxies, which are best described by de Vaucouleurs-like profiles ( $n \sim 4-5$ ). The difference in source and lens morphologies supports the expectation that quasar host galaxies at moderate redshift can exhibit more diverse and irreg-

ular structures compared to the typically more evolved lensing galaxies (Peng et al. 2006).

Moreover, the presence of extended host emission substantially improves the recovery of the Fermat potential by introducing additional constraints on the lensing deflection angles across the image plane. This is particularly evident in J1620+1203 and J2325-5229, where the well-resolved arcs trace out the lens potential beyond the limited positional constraints from only the quasar images. As a result, these systems, especially J1620+1203 and J2325-5229, are promising candidates for future time-delay cosmography studies aimed at constraining the Hubble constant.

#### 4.5. Time Delay Parameters

**Table 6.** Median Fermat potential differences between quasar images and subsequent predicted time delays using the measured redshifts. The associated uncertainties are statistical and were calculated using the 84th and 16th percentiles. For these calculations, we assume a flat  $\Lambda$ CDM cosmology with  $H_0 = 70 \text{ km s}^{-1} \text{ Mpc}^{-1}$ ,  $\Omega_{m,0} = 0.3$ , and  $\Omega_{\Lambda,0} = 0.7$ .

Lens System	$z_l$	$z_s$	$\Delta\Phi_{AB}$	$\Delta t_{AB}$ [days]
J0407-5006	0.55	1.515	$0.925^{+0.016}_{-0.028}$	$99.5^{+1.7}_{-3.0}$
J0806+2006	0.573	1.54	$-0.468^{+0.023}_{-0.010}$	$-53.3^{+2.6}_{-1.2}$
J1442+4055	0.284	2.593	$-0.655^{+0.007}_{-0.015}$	$-25.8^{+0.3}_{-0.6}$
J1515+1511	0.742	2.049	$-1.188^{+0.020}_{-0.026}$	$-174.9^{+3.0}_{-3.8}$
J1620+1203	0.398	1.158	$2.453^{+0.071}_{-0.080}$	$183.2^{+5.3}_{-6.0}$
J2325-5229	0.40	2.739	$-0.712^{+0.031}_{-0.024}$	$-41.5^{+1.8}_{-1.4}$

Table 6 presents the median Fermat potential differences,  $\Delta\Phi_{AB}$ , between image pairs, alongside the resulting time delays,  $\Delta t_{AB}$ , computed under an assumed flat  $\Lambda$ CDM cosmology with  $H_0 = 70 \text{ km s}^{-1} \text{ Mpc}^{-1}$ , a matter density  $\Omega_{m,0} = 0.3$ , and a dark energy density  $\Omega_{\Lambda,0} = 0.7$ . The quoted uncertainties represent statistical errors propagated from the posterior distributions of the lens model parameters. For clarity, we define the time delay difference as:

$$\Delta t_{AB} = t_A - t_B, \quad (14)$$

such that  $\Delta t_{AB}$  is negative when the information from Image A arrives before Image B.

The calculated Fermat potential differences span a broad range, from  $|\Delta\Phi_{AB}| \sim 0.47$  (J0806+2006) to  $|\Delta\Phi_{AB}| \sim 2.45$  (J1620+1203), reflecting the diverse lensing geometries and mass distributions within our sample. The corresponding time delays, which also depend on the lens and source redshifts, range from a few tens of days to over 180 days. J1620+1203, in particular, exhibits the largest predicted delay at  $\Delta t_{AB} = 183.2^{+5.3}_{-6.0}$  days, owing to both its steep Fermat potential gradient and relatively favorable redshift configuration. Such long delays are especially advantageous for time-delay cosmography, as they mitigate the impact of seasonal observing gaps and improve the signal-to-noise of the lag measurement. Conversely, the shortest time delay is observed in J1442+4055, with  $\Delta t_{AB} = -25.8^{+0.3}_{-0.6}$  days, despite a relatively high source redshift. This highlights the dominant role of the lens mass profile and angular configuration in shaping the time-delay landscape. Negative time delays, as seen in systems like J0806+2006 and J1515+1511, correspond to the arrival of image B before image A, consistent with the relative Fermat potential differences.

Notably, four of our time delay calculations match their observational counterparts within  $1\sigma$ :

1. *J0806+2006*: The calculated value of  $\Delta t_{AB} = -53.3^{+2.6}_{-1.2}$  days is in precise agreement with the observed  $\Delta t_{AB} = -53.0^{+6.0}_{-6.0}$  days presented in [Bekov et al. \(2024\)](#).

2. *J1442+4055*: The calculated value of  $\Delta t_{AB} = -25.8^{+0.3}_{-0.6}$  is in agreement with the observed value of  $\Delta t_{AB} = -25.0^{+1.5}_{-1.5}$  detailed in [Shalyapin & Goicoechea \(2019\)](#).
3. *J1620+1203*: Our model of  $\Delta t_{AB} = 183.2^{+5.3}_{-6.0}$  days is in agreement with the  $\Delta t_{AB} = 171.5^{+8.7}_{-8.7}$  days measurement from [Millon et al. \(2020\)](#).
4. *J2325-5229*: Our calculation of  $\Delta t_{AB} = -41.5^{+1.8}_{-1.4}$  days is in agreement with the observed  $\Delta t_{AB} = -52^{+11}_{-11}$  days presented in [Ostrovski et al. \(2017\)](#).

For J0407-5006, there is no published observed time delay data. For J1515+1511, our calculation of  $\Delta t_{AB} = -174.9^{+3.0}_{-3.8}$  days is not in agreement with the presented observational measurement of  $\Delta t_{AB} = -211^{+5.0}_{-5.0}$  from [Shalyapin & Goicoechea \(2017\)](#). These results further support the vigorousness of our modeling pipeline.

## 5. DISCUSSION

In this section, we discuss systematics that may alter the accuracy of our lens models and results.

### 5.1. The Point Spread Function

A potentially significant source of uncertainty in our analysis arises from the characterization and modeling of the PSF. The HST PSF varies spatially across the field of view and temporally with changes in focus and optical alignment ([Anderson & King 2006](#)). For our purposes, small mismatches between the empirical or model PSF and the true PSF at the position of each quasar image introduce systematic errors in flux estimation and centroid determination.

Techniques such as drizzling ([Fruchter & Hook 2002](#)) and sub-pixel dithering help mitigate undersampling but do not eliminate PSF mismatch errors entirely. Similarly, the accuracy of the PSF is inherently limited by the signal-to-noise ratio of the calibration data and by the interpolation scheme used to build a position-dependent model. As noted by [Bellini & Bedin \(2009\)](#),

even in carefully calibrated PSF libraries, position-dependent variations can introduce astrometric biases at the level of  $\sim 1.0$  mas for WFC3.

To help mitigate these effects, our observations employed a 2-point dither pattern designed to provide sub-pixel sampling of the PSF and to reduce aliasing artifacts introduced by the detector's undersampling. Additionally, we constructed empirical PSFs directly from the dithered science exposures using isolated stars in the field whenever available. These PSFs were then iteratively refined throughout the modeling process (as described in Section 3.2) to more accurately fit the quasar images. While this approach does not eliminate PSF uncertainties, it allows for partial correction of spatial variations and reduces systematic residuals in the model fitting.

### 5.2. Cosmological Model Dependence

An important caveat in our time delay analysis is the assumption of a flat  $\Lambda$ CDM cosmology with fixed parameters  $H_0 = 70 \text{ km s}^{-1} \text{ Mpc}^{-1}$ ,  $\Omega_{m,0} = 0.3$ , and  $\Omega_{\Lambda,0} = 0.7$ . While this choice is motivated by its broad acceptance and consistency with multiple cosmological probes, it inherently biases our predicted time delays. Specifically, the time-delay distance,  $D_{\Delta t}$ —which scales the Fermat potential difference to a physical delay—depends sensitively on the underlying cosmological parameters, particularly  $H_0$  and the matter-energy density parameters (Refsdal 1964; Suyu et al. 2010). Variations in these parameters can induce percent-level to tens-of-percent shifts in predicted delays, as emphasized by Wong et al. (2020) in the H0LiCOW results.

By anchoring the model to a specific cosmology, we effectively suppress cosmological variance and implicitly assume that any discrepancies between predicted and observed time delays stem solely from lens modeling inaccuracies or measurement noise. This neglects the fact that time-delay cosmography is fundamentally sensitive to cosmological model choices. For instance, models with non-zero curvature or evolving dark energy components would yield systematically different delay predictions for the same Fermat potential (Birrer et al. 2020). Moreover, adopting fixed cosmological parameters during model testing can bias lens reconstructions by coupling astrophysical and cosmological uncertainties.

While our primary goal here is to test the internal consistency of lens model predictions rather than perform cosmological inference, we note that future improvements would benefit from marginalizing over a broader range of cosmologies, as done in fully Bayesian time-delay cosmography (Treu & Marshall 2016). This

would allow a more honest appraisal of systematic uncertainties tied to cosmological assumptions and provide a pathway for integrating independent cosmological priors. Nonetheless, under the most widely agreed upon cosmological model, four out of five of our results remain within  $1\sigma$  of observations, thus supporting the vigor of our pipeline.

## 6. CONCLUSIONS AND FUTURE WORK

In this work, we have developed and validated a comprehensive framework for modeling doubly imaged quasar strong gravitational lensing systems, with a particular emphasis on preparing for time-delay cosmography analyses. Using the open-source software `Lenstronomy` across two HST bands, we constructed lens models that jointly fit the mass profiles of the deflector galaxies, the point-like quasar images, and, where applicable, the extended emission from the source galaxy. The resulting models yield Sérsic indices and effective radii consistent with early-type lens morphologies, image separations indicative of galaxy-scale lenses, and a wide range of flux ratios shaped by lensing magnification and potential microlensing.

Modeling the lens light in both the F814W and F475X bands revealed small but systematic differences: effective radii and Sérsic indices tend to be slightly lower in the F475X band, suggesting the presence of redder stellar populations indicative of early-type galaxies at modest redshift. The lens mass models, characterized by their Einstein radii, mass ellipticities, and external shear, show that the systems are dominated by massive central galaxies with little to no environmental influences. Three systems (J0806+2006, J1620+1203, and J2325-5229) show evidence of extended source light in the F814W band, enabling the reconstruction of the quasar host galaxy's morphology and providing additional constraints on the lens mass distribution. The source profiles recovered in these systems exhibit low Sérsic indices and varying ellipticity, consistent with irregular structures at modest redshifts.

Following the construction of the lensing systems through our pipeline, calculations of the Fermat potential and time delay differences between quasar images are calculated blindly in a flat  $\Lambda$ CDM cosmology and then compared with observational data of said system. Four out of five systems match observational results within  $1\sigma$ , while J0407-5006 does not have quasar image light curve data. This consistency between modeled and observed time delays serves as a strong validation of our pipeline's accuracy in reconstructing lensing configurations and inferring cosmological observables.

The next phase of this work will seek to incorporate the measured time delays with the calculated Fermat potentials to compute the time-delay distances for each lens system and thereby the Hubble constant. To fully exploit the cosmological information, we will employ a hierarchical Bayesian framework that combines the time-delay distance measurements from multiple systems to jointly infer  $H_0$  and quantify systematic uncertainties. This hierarchical approach will enable us to propagate modeling uncertainties and capture the intrinsic scatter between different lens systems, resulting in a robust and transparent estimation of  $H_0$ . Ultimately, this methodology will contribute to the broader effort to resolve the current tension in Hubble constant measurements and potentially reveal new physics beyond the standard cosmological model.

<sup>1</sup> **Lenstronomy** is open source and freely available at <https://github.com/lenstronomy/lenstronomy>. All notebooks detailing the lens modeling procedure and analysis are available at [https://github.com;bradyryan/hst\\_doubles](https://github.com;bradyryan/hst_doubles). The work at Stony Brook was supported by the National Aeronautics and Space Administration (NASA) New York Space Grant Consortium.

#### Facilities: Seawulf

**Software:** AstroDrizzle (Avila et al. 2015), emcee (Foreman-Mackey et al. 2013), Jupyter (Kluyver et al. 2016), **Lenstronomy** (Birrer & Amara 2018), matplotlib (Hunter 2007), Numpy (van der Walt et al. 2011), SExtractor (Bertin & Arnouts 1996), STARRED (Millon et al. 2024).

## REFERENCES

Anderson, J., & King, I. R. 2006, PSFs, Photometry, and Astronomy for the ACS/WFC, Instrument Science Report ACS 2006-01, 34 pages

Anguita, T., Schechter, P. L., Kuropatkin, N., et al. 2018, Monthly Notices of the Royal Astronomical Society, 480, 5017, doi: [10.1093/mnras/sty2172](https://doi.org/10.1093/mnras/sty2172)

Avila, R., Koekemoer, A., Mack, J., & Fruchter, A. 2015, Optimizing pixfrac in Astrodrizzle: An example from the Hubble Frontier Fields, Instrument Science Report WFC3 2015-04, 17 pages

Bajaj, V., Calamida, A., & Mack, J. 2020, Updated WFC3/IR Photometric Calibration, Instrument Science Report WFC3 2020-10, 19 pages

Bekov, D. K., Akhunov, T. A., Burkhanov, O. A., & Alimova, N. R. 2024, Astrophysical Bulletin, 79, 15, doi: [10.1134/S1990341323600278](https://doi.org/10.1134/S1990341323600278)

Bellini, A., & Bedin, L. R. 2009, PASP, 121, 1419, doi: [10.1086/649061](https://doi.org/10.1086/649061)

Bertin, E., & Arnouts, S. 1996, A&AS, 117, 393, doi: [10.1051/aas:1996164](https://doi.org/10.1051/aas:1996164)

Birrer, S., & Amara, A. 2018, Physics of the Dark Universe, 22, 189, doi: <https://doi.org/10.1016/j.dark.2018.11.002>

Birrer, S., Treu, T., Rusu, C. E., et al. 2019, MNRAS, 484, 4726, doi: [10.1093/mnras/stz200](https://doi.org/10.1093/mnras/stz200)

Birrer, S., Shajib, A. J., Galan, A., et al. 2020, A&A, 643, A165, doi: [10.1051/0004-6361/202038861](https://doi.org/10.1051/0004-6361/202038861)

Birrer, S., Millon, M., Sluse, D., et al. 2024, SSRv, 220, 48, doi: [10.1007/s11214-024-01079-w](https://doi.org/10.1007/s11214-024-01079-w)

Di Valentino, E., Mena, O., Pan, S., et al. 2021, Classical and Quantum Gravity, 38, 153001, doi: [10.1088/1361-6382/ac086d](https://doi.org/10.1088/1361-6382/ac086d)

Faber, S. M., & Jackson, R. E. 1976, ApJ, 204, 668, doi: [10.1086/154215](https://doi.org/10.1086/154215)

Foreman-Mackey, D., Hogg, D. W., Lang, D., & Goodman, J. 2013, PASP, 125, 306, doi: [10.1086/670067](https://doi.org/10.1086/670067)

Fruchter, A. S., & Hook, R. N. 2002, PASP, 114, 144, doi: [10.1086/338393](https://doi.org/10.1086/338393)

Hunter, J. D. 2007, Comput. Sci. Eng., 9, 90, doi: [10.1109/mcse.2007.55](https://doi.org/10.1109/mcse.2007.55)

Inada, N., Oguri, M., Becker, R. H., et al. 2006, AJ, 131, 1934, doi: [10.1086/500591](https://doi.org/10.1086/500591)

Kayo, I., Inada, N., Oguri, M., et al. 2010, AJ, 139, 1614, doi: [10.1088/0004-6256/139/4/1614](https://doi.org/10.1088/0004-6256/139/4/1614)

Kluyver, T., Ragan-Kelley, B., Pérez, F., et al. 2016, in Positioning and Power in Academic Publishing: Players, Agents and Agendas, ed. F. Loizides & B. Schmidt, IOS Press, 87 – 90

Liao, K., Treu, T., Marshall, P., et al. 2015, ApJ, 800, 11, doi: [10.1088/0004-637X/800/1/11](https://doi.org/10.1088/0004-637X/800/1/11)

Millon, M., Michalewicz, K., Dux, F., Courbin, F., & Marshall, P. J. 2024, AJ, 168, 55, doi: [10.3847/1538-3881/ad4da7](https://doi.org/10.3847/1538-3881/ad4da7)

Millon, M., Courbin, F., Bonvin, V., et al. 2020, A&A, 640, A105, doi: [10.1051/0004-6361/202037740](https://doi.org/10.1051/0004-6361/202037740)

More, A., Cabanac, R., More, S., et al. 2012, ApJ, 749, 38, doi: [10.1088/0004-637X/749/1/38](https://doi.org/10.1088/0004-637X/749/1/38)

Oguri, M., & Marshall, P. J. 2010, MNRAS, 405, 2579, doi: [10.1111/j.1365-2966.2010.16639.x](https://doi.org/10.1111/j.1365-2966.2010.16639.x)

Ostrovski, F., McMahon, R. G., Connolly, A. J., et al. 2017, MNRAS, 465, 4325, doi: [10.1093/mnras/stw2958](https://doi.org/10.1093/mnras/stw2958)

Peng, C. Y., Impey, C. D., Rix, H.-W., et al. 2006, ApJ, 649, 616, doi: [10.1086/506266](https://doi.org/10.1086/506266)

Planck Collaboration, Aghanim, N., Akrami, Y., et al. 2020, *A&A*, 641, A6, doi: [10.1051/0004-6361/201833910](https://doi.org/10.1051/0004-6361/201833910)

Refsdal, S. 1964, *MNRAS*, 128, 307, doi: [10.1093/mnras/128.4.307](https://doi.org/10.1093/mnras/128.4.307)

Richards, G. T., Lacy, M., Storrie-Lombardi, L. J., et al. 2006, *ApJS*, 166, 470, doi: [10.1086/506525](https://doi.org/10.1086/506525)

Riess, A. G., Yuan, W., Macri, L. M., et al. 2022, *ApJL*, 934, L7, doi: [10.3847/2041-8213/ac5c5b](https://doi.org/10.3847/2041-8213/ac5c5b)

Schmidt, T., Treu, T., Birrer, S., et al. 2023, *MNRAS*, 518, 1260, doi: [10.1093/mnras/stac2235](https://doi.org/10.1093/mnras/stac2235)

Shalyapin, V. N., & Goicoechea, L. J. 2017, *ApJ*, 836, 14, doi: [10.3847/1538-4357/836/1/14](https://doi.org/10.3847/1538-4357/836/1/14)

—. 2019, *ApJ*, 873, 117, doi: [10.3847/1538-4357/ab08f0](https://doi.org/10.3847/1538-4357/ab08f0)

Sonnenfeld, A., Treu, T., Gavazzi, R., et al. 2013, *ApJ*, 777, 98, doi: [10.1088/0004-637X/777/2/98](https://doi.org/10.1088/0004-637X/777/2/98)

Suyu, S. H., Marshall, P. J., Auger, M. W., et al. 2010, *ApJ*, 711, 201, doi: [10.1088/0004-637X/711/1/201](https://doi.org/10.1088/0004-637X/711/1/201)

Suyu, S. H., Bonvin, V., Courbin, F., et al. 2017, *MNRAS*, 468, 2590, doi: [10.1093/mnras/stx483](https://doi.org/10.1093/mnras/stx483)

Treu, T., & Marshall, P. J. 2016, *The Astronomy and Astrophysics Review*, 24, doi: [10.1007/s00159-016-0096-8](https://doi.org/10.1007/s00159-016-0096-8)

Treu, T., Agnello, A., Baumer, M. A., et al. 2018, *Monthly Notices of the Royal Astronomical Society*, 481, 1041, doi: [10.1093/mnras/sty2329](https://doi.org/10.1093/mnras/sty2329)

van der Walt, S., Colbert, S. C., & Varoquaux, G. 2011, *Comput. Sci. Eng.*, 13, 22, doi: [10.1109/mcse.2011.37](https://doi.org/10.1109/mcse.2011.37)

Weinberg, D. H., Mortonson, M. J., Eisenstein, D. J., et al. 2013, *PhR*, 530, 87, doi: [10.1016/j.physrep.2013.05.001](https://doi.org/10.1016/j.physrep.2013.05.001)

Wong, K. C., Suyu, S. H., Chen, G. C. F., et al. 2020, *MNRAS*, 498, 1420, doi: [10.1093/mnras/stz3094](https://doi.org/10.1093/mnras/stz3094)